Unveiling the hidden intrinsic porosity of marine biomass-derived carbon: Eliminating pore-blocking minerals

He, Da
Interdisciplinary Graduate School of Engineering Sciences, Kyushu University

Saito, Koji
Nippon Steel Research Institute Corporation

Kato, Toru
Environment and Process Research Department, The Japan Research and Development Center for Metals

Kosugi, Chika
Advanced Technology Research Laboratories, Nippon Steel Corporation

他

出版情報：Carbon Reports. 3 (1), pp.18-28, 2024-03-01. 炭素材料学会
バージョン：

Carbon Reports
Vol. 3 No. 1 2024 18-28

Research Paper

Unveiling the hidden intrinsic porosity of marine biomass-derived carbon: Eliminating pore-blocking minerals

Da He[a)], Koji Saito[b)], Toru Kato[c)], Chika Kosugi[d)], Takaaki Shimohara[e)], Koji Nakabayashi[a),e)], Seong-Ho Yoon[a),e)] and Jin Miyawaki[a),e),*]

a) Interdisciplinary Graduate School of Engineering Sciences, Kyushu University: 6–1 Kasuga-koen, Kasuga, Fukuoka 816–8580, Japan
b) Nippon Steel Research Institute Corporation: 2–6–1 Marunouchi, Chiyoda-ku, Tokyo 100–0005, Japan
c) Environment and Process Research Department, The Japan Research and Development Center for Metals: 1–5–11 Nishishinbashi, Minato-ku, Tokyo 105–0003, Japan
d) Advanced Technology Research Laboratories, Nippon Steel Corporation: 20–1 Shintomi, Futtsu, Chiba 293–8511, Japan
e) Institute for Materials Chemistry and Engineering, Kyushu University: 6–1 Kasuga-koen, Kasuga, Fukuoka 816–8580, Japan

In the pursuit of carbon neutrality, marine biomass (MB) has emerged as a promising alternative to traditional carbon sources. This study endeavors to establish an economically viable pathway to derive porous carbon materials from MB. Simple pyrolysis of MB resulted in a MB-based carbon (MBC) characterized by a negligible open-pore structure. However, subsequent water washing transformed it into a porous material. N_2 adsorption tests revealed that the pyrolysis temperature and washing method substantially influenced the specific surface area (SSA) and pore volume of the MBC. While the catalytic activation function of elements inherent in MB, such as Na, Mg, K, Ca, and Cl, rendered MBC inherently porous, these elements also induced an initial pore-blocking effect that concealed the pores. Subsequent washing with water nearly eradicated Na, K, and Cl from MBC, making a number of the concealed pores accessible. Furthermore, a CO_2 aeration washing method effectively eliminated Mg and Ca elements from MBC, resulting in a substantial increase in SSA (>1000 m^2/g) without the need for additional activation processes. Based on an understanding of the dual role of the elements naturally present in MB, this study demonstrates a potential strategy for environmentally friendly and cost-effective porous carbon production.

KEYWORDS : Marine biomass, Porous carbon, Porosity, Dual role, Mineral

1. Introduction

Activated carbon (AC), a representative porous carbon material, stands as a well-established industrial product with extensive application prospects in various fields, including catalysis [1–3], adsorption [4–6], and environmental remediation [7, 8]. This popularity is attributed to its highly developed porous structure, stemming from the raw material/precursor and activation process [9]. To broaden and enhance the performance of porous carbon materials, substantial research efforts have been dedicated to choosing and designing raw materials/precursors and preparation processes. The goal is to obtain carbon materials with diverse porous structures, catering to different application scenarios.

Carbon materials with extensive pore structures are typically derived from specific raw materials or intricate synthesis processes. For instance, hierarchical porous structures are achieved from organic precursors or charcoal through physical or chemical activation [10]. Mesoporous AC, prepared by the chemical activation of charcoal, has found application in high-strength lithium battery electrodes [11]. However, this approach is not always sustainable due to the inefficient source of its precursor and/or the accompanying large amount of CO_2 emissions during the pyrolysis and activation process [12]. Furthermore, although chemical activation can afford a high degree of pore development, the requirement of acid-washing post-treatment increases production costs and pollutes wastewater. On the other hand, we have proposed a simple preparation method for AC with highly developed porosity through pressurized physical activation using CO_2 as an activating gas [13]. We have demonstrated the high performance of the derived AC as an adsorbent in an adsorption heat pump system [14]. Unlike chemical activations, this method is free from the problem of polluted wastewater; however, the activation process itself, coupled with the need for pressure-tight equipment,

* Corresponding Author, E-mail: miyawaki@cm.kyushu-u.ac.jp
https://doi.org/10.7209/carbon.030102
(Received November 7, 2023, Accepted December 19, 2023)
(J-STAGE Advance published December 28, 2023)

may increase production costs. Apart from activation methods, template methods have been reported to obtain porous carbon materials with well-regulated pore structures. The hard template method uses fluid organic matter as a raw material to prepare mesoporous carbon [15, 16]. In contrast, the soft template method uses organic monomers to produce microporous carbon spheres [17–19]. Some raw materials are costly in these cases, and the synthesis process is typically complex, toxic, expensive, time-consuming, and energy-consuming. In the context of CO_2 reduction in the industrial sector, the development of alternative environmentally friendly strategies is urgently required to obtain mature porous carbon-based industrial products from sustainable raw materials.

Marine biomass (MB) showcases distinctive characteristics among current raw materials owing to its ultrahigh photosynthetic efficiency compared to terrestrial biomass [20, 21]. Consequently, it can result in a heightened CO_2 absorption rate and increased organic matter production, thereby advancing the realization of carbon neutrality objectives in the porous carbon industry. Simultaneously, the easily extractable and non-soil-damaging attributes of MB make it suitable for extensive promotion. Capitalizing on these advantages, MB has garnered substantial global research attention as a potential substitute for traditional raw materials in porous carbon productions [22, 23]. For instance, Boubakri *et al.* have crafted a porous carbon through activation in an alkaline medium, utilizing MB as a raw material, showcasing a microstructure characterized by hollow spheres [24]. The outcomes in heavy metal adsorption were remarkable. In electrochemical applications, highly ordered microporous/macroporous AC has been fabricated using marine algae as raw material through slow pyrolysis and nitric acid activation techniques and subsequently applied to supercapacitors [25]. Nonetheless, ongoing research on MB-derived porous carbon production remains confined to expensive activation methods tailored for specific MB species, limiting widespread industrial applications. Hence, the central challenge lies in devising cost-effective and low environmental burden strategies to regulate the porosity of MB-based carbon (MBC) for versatile adaptation across various industrial applications [26, 27].

In this study, we found that low-temperature carbonized MB inherently possesses porosity. However, mineral crystals, including alkaline and alkaline earth metals and chlorine, impede access to developed pores. Utilizing a simple water-washing method and a unique CO_2 aeration technique, proven more effective than pure water washing [28], removes these minerals. This reveals intrinsic pores, yielding porous MBC with a specific surface area (SSA) higher than 1000 m^2/g without additional activation processes.

2. Experimental

2.1 Preparation of MB-based carbon (MBC) and porous MBC

This study employed two seaweed types, *Luminaria* (Kombu, KB) and *Undaria pinnatifida* (Wakame, WKM), sourced from Japan's coastal regions. NIPPON STEEL CORPORATION provided MB samples. To prepare the samples, MB samples underwent initial drying at 90 °C and subsequent pulverization to a size below 250 µm (abbreviated as Raw-WKM and Raw-KB). Elemental composition analysis (CHN-Coder; MT-5, Yanako, Kyoto, Japan) revealed the basic element characteristics: For Raw-WKM, carbon: 31.6 mass%, hydrogen: 5.3 mass%, nitrogen: 1.9 mass%, and ash: 8.7 mass%. For Raw-KB: carbon: 31.6 mass%, hydrogen: 5.4 mass%, nitrogen: 1.5 mass%, and ash: 8.7 mass%. Carbonized samples were derived from each MB powder through pyrolysis under an N_2 atmosphere for 2 h at temperatures ranging from 600 °C to 1000 °C. The resulting MBC products are denoted as WKMx and KBx, with x=600, 800, 850, 900, 950, or 1000, representing the respective pyrolysis temperatures (in °C).

Fig. 1 illustrates the preparation and impurity removal process for both WKMx and KBx. To eliminate impurities using the water-washing method, 0.5 g of WKMx or KBx was dispersed in deionized water (500 mL), stirred for 2 h, filtered, and dried at 90 °C. The resulting specimens were labeled as WKMx-WT and KBx-WT, respectively. Conversely, if CO_2 gas was introduced during the stirring

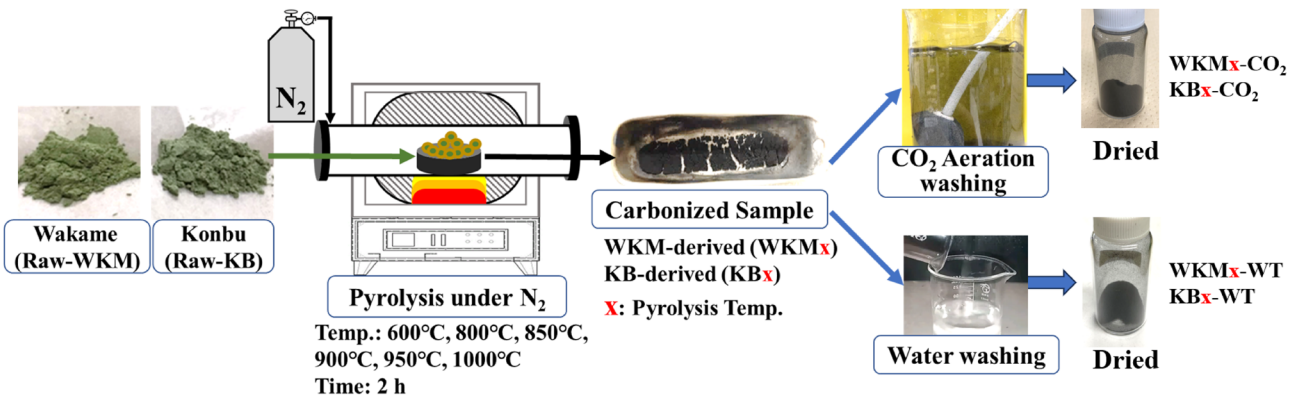

Fig. 1 Preparation and impurity removal from MB-based carbons.

process at a gas flow rate of 100 mL/min, that is, in the case of the CO_2 aeration washing method, the obtained samples were denoted as WKMx-CO_2 and KBx-CO_2, respectively.

2.2 Characterization of MBC and porous MBC

Specific surface morphology was observed through scanning electron microscopy (SEM; JSM-6700F; JEOL, Japan) equipped with an energy-dispersive spectrometer (EDS; Smartedx, Oxford Instruments, UK) for mapping within the scanning area. The pyrolysis process of raw and carbonized MB samples was characterized using thermogravimetric analysis (TGA; STA2500 Regulus, NETZSCH, Germany). Elemental compositions were examined *via* X-ray fluorescence spectrometry (XRF; ZSX Primus IV/RX9, Rigaku, Japan). N_2 adsorption and desorption isotherms were measured at 77 K using a volumetric physisorption apparatus (Nova 2000E; Anton Paar Quantachrome Instruments, USA). SSA was calculated using the α_S-plot method based on the N_2 adsorption data [29, 30]. The pore size distribution (PSD) and pore volume were determined using the non-local density functional theory (NLDFT) assuming a slit-shaped pore [31].

3. Results and Discussion

3.1 Preliminary examination of intrinsic porosity of MBC using WKM600 and WKM600-WT

The study commences with a preliminary examination utilizing low-temperature carbonized MB (WKM600) and the corresponding water-washed MBC (WKM600-WT) as test samples. **Fig. 2** illustrates the N_2 adsorption and desorption isotherms at 77 K for WKM600 and WKM600-WT. The adsorption curve for the carbonized sample, WKM600, appeared nearly as a parallel line with negligible adsorption capacity, implying the absence of a pore structure. However, after the water-washing process, WKM600-WT exhibited a notable N_2 adsorption capacity, highlighting that MBC inherently possesses a pore structure. In other words, water washing facilitated the transition of latent pores into open pores, suggesting a possibility of pore-blocking by water-soluble substances in MBC.

Previous studies have indicate that MB can attain a satisfactory pore structure through high-temperature pyrolysis. However, the water-washed MB precursor loses this pore-formation ability during subsequent pyrolysis [24]. This observation strongly implies that water-soluble substances within MB contribute to pore formation. Nevertheless, the precise mechanisms governing pore formation and the newly identified pore-blocking effect in WKM600 have not been elucidated.

3.2 Pore structure analysis of the MBC

If achieving exceptional porous characteristics in MBC through simple pyrolysis proves feasible, it could enhance its potential as an industrial porous carbon material with a reduced environmental footprint. Therefore, this study now undertakes systematic investigations

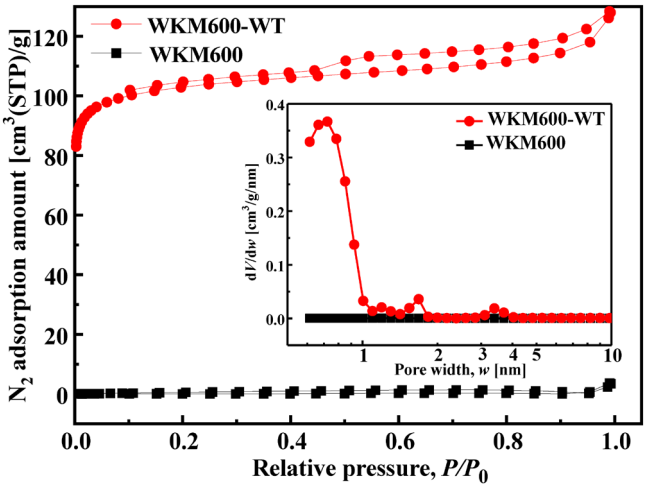

Fig. 2 N_2 adsorption and desorption isotherms at 77 K of low-temperature (600 °C) carbonized WKM before and after water washing. Inset: NLDFT pore size distribution.

based on the preliminary examination's findings, particularly emphasizing pyrolysis (carbonization) temperature and washing methods. The primary objective of this study revolves around exploring the inherent porous structures and understanding the mechanisms governing both pore formation and pore-blocking within MBC.

In **Figs. 3** and **S1** in the Supporting Information, N_2 adsorption and desorption isotherms at 77 K are presented for MBC obtained at various carbonization temperatures ranging from 800 °C to 1000 °C and the corresponding washed MBC samples. The adsorption capacity of WKM800 was notably constrained, indicating a deficiency in its porous characteristics. However, the other samples exhibited typical characteristics of a Type I isotherm with a Type H4 hysteresis loop in the IUPAC classification [30]. Type I isotherms are commonly observed in microporous materials like molecular sieves and microporous carbon materials. They manifest as a rapid increase in adsorption capacity at low relative pressure (P/P_0), reaching saturation above a certain P/P_0. Furthermore, the Type H4 hysteresis loop observed at P/P_0=0.45–0.90 indicated the presence of mesopores.

Irrespective of the carbonization temperature and the raw MB species, the saturated N_2 adsorption capacity showed the lowest value in the carbonized samples, followed by the water-washed samples and then the CO_2-aeration-washed samples. To illustrate changes in pore structure clearly, the α_S-plot method was employed to calculate SSA. The blue curve in **Fig. 3**(f) demonstrates that the carbonized MB samples (WKMx) increased SSA as the carbonization temperature rose. This indicates the creation of pore structures through pyrolysis and/or the partial removal of pore-blocking effects by high temperatures. After water washing, the overall increase in SSA indicates an unveiling of intrinsic pores of MBC through the removal of water-soluble pore-blocking substances (red curve in **Fig. 3**(f)), as detailed in the previous section. However, with increased carbonization temperature, the SSA of WKMx-WT did not consistently increase,

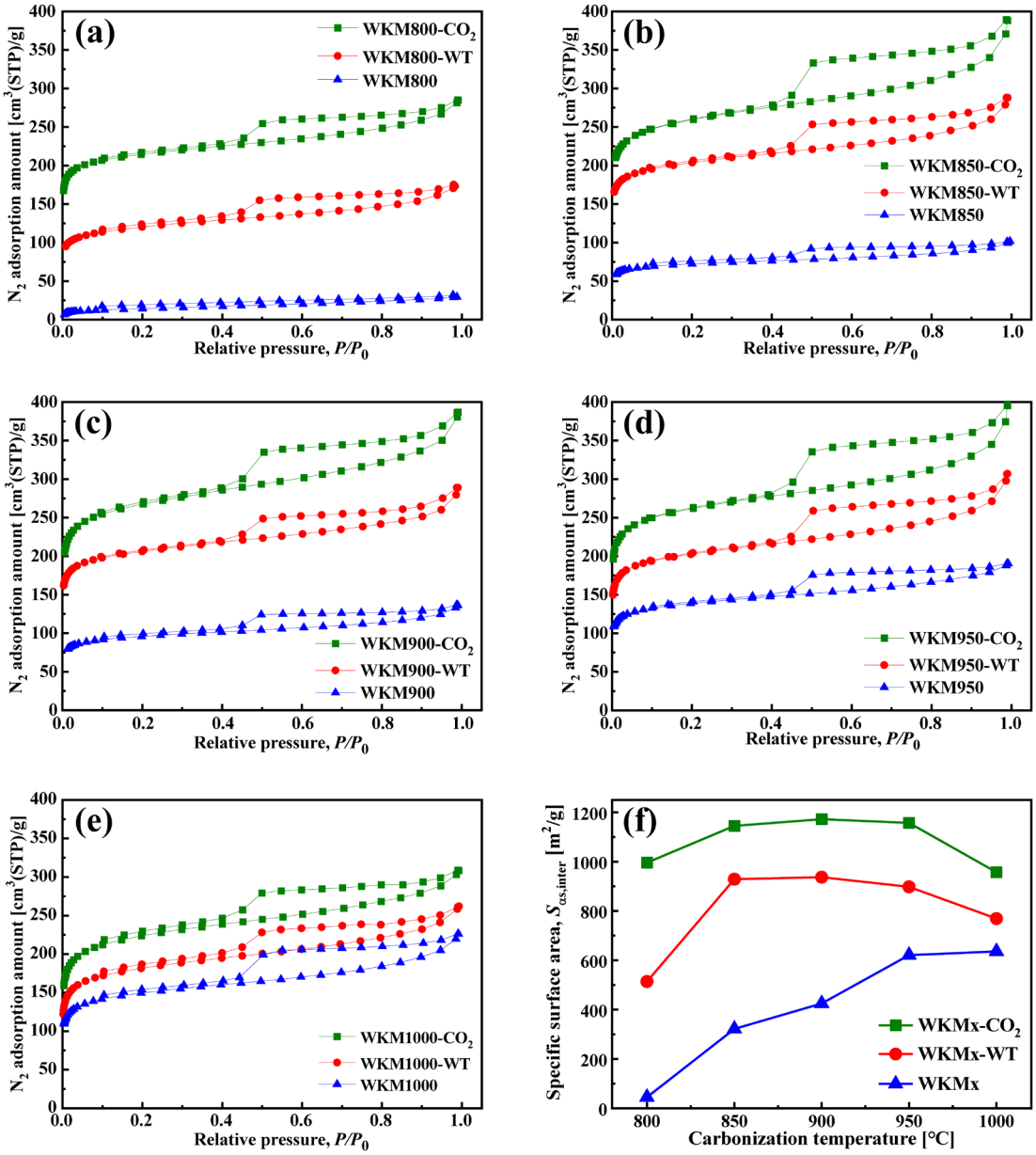

Fig. 3 N_2 adsorption and desorption isotherms at 77 K for WKMx, WKMx-WT, and WKM-CO_2 at varied carbonization temperatures of (a) 800 °C, (b) 850 °C, (c) 900 °C, (d) 950 °C, and (e) 1000 °C. (f) Comparative analysis of internal SSA using the α_S-plot method for all WKM-derived samples.

indicating that excessive temperature may cause the existing pore structure to shrink or collapse. After CO_2 aeration washing, the SSA values of any WKMx-CO_2 sample further increased (green curve in **Fig. 3**(f)), indicating that although water washing can unveil a portion of the intrinsic pores of MBC, CO_2 aeration washing can more deeply release the pore structure. Similar to the case of WKMx-WT, as the carbonization temperature increased, the SSA of WKMx-CO_2 did not always increase but reached its peak at around 900 °C, indicating the presence of the optimum carbonization temperature to obtain the porous MBC sample with the maximum SSA value.

Comparable observations were noted in carbonized samples utilizing KB as the raw material (see **Fig. S1** in the Supporting Information). The CO_2-aeration-washed samples exhibited the highest SSA, succeeded by the water-washed samples and then the carbonized samples. In the case of KBx-CO_2, the highest SSA was likewise achieved within the carbonization temperature range of 850–950 °C.

The calculated results for SSA and total pore volume (V_{total}) are presented in **Table 1**. A consistent trend in V_{total} values mirrored that of SSA: carbonized samples exhibited the lowest values, followed by water-washed and CO_2-aeration-washed samples. For instance, the total pore volume of carbonized WKM samples was 0.31 cm^3/g at most. In contrast, water washing resulted in a total pore volume of 0.41 cm^3/g, while CO_2 aeration washing increased the total pore volume to a maximum of 0.54 cm^3/g. Although WKM1000 displayed the highest V_{total} and SSA values, the carbonization temperature at 900–950 °C yielded the highest values for water-washed or CO_2-aera-

Table 1 Pore structural parameters estimated from N_2 adsorption isotherms at 77 K of WKM-derived samples.

Samples	$S_{\alpha s,total}$ [m^2/g] [a]	$S_{\alpha s,inter}$ [m^2/g] [b]	V_{total} [cm^3/g] [c]	V_{micro} [cm^3/g] [d]	V_{micro}/V_{total} [%] [e]
WKM800	48	45	0.04	0.02	50
WKM850	330	322	0.14	0.10	71
WKM900	436	425	0.19	0.13	68
WKM950	633	621	0.26	0.18	69
WKM1000	657	636	0.31	0.19	61
WKM800-WT	536	514	0.24	0.15	62
WKM850-WT	949	929	0.39	0.26	67
WKM900-WT	958	937	0.39	0.27	69
WKM950-WT	922	898	0.41	0.25	61
WKM1000-WT	792	769	0.36	0.23	64
WKM800-CO_2	1014	996	0.39	0.28	72
WKM850-CO_2	1177	1145	0.53	0.32	60
WKM900-CO_2	1198	1172	0.53	0.34	64
WKM950-CO_2	1189	1157	0.54	0.32	59
WKM1000-CO_2	980	957	0.42	0.29	69

[a] $S_{\alpha s,total}$: Total specific surface area obtained using the α_S-plot method.
[b] $S_{\alpha s,inter}$: Internal specific surface area calculated from the equation, $S_{\alpha s,inter}=S_{\alpha s,total}-S_{\alpha s,exter}$, where the external SSA ($S_{\alpha s,exter}$) was determined by the α_S-plot method.
[c] V_{total}: Total pore volume obtained using the NLDFT method.
[d] V_{micro}: Micropore volume obtained using the NLDFT method.
[e] V_{micro}/V_{total}: Micropore volume ratio.

tion-washed samples. This observation indicates that 900–950 °C was optimal for introducing intrinsic pores through pyrolysis. The same conclusion held true for carbonized samples using KB as a precursor (see **Table S1** in the Supporting Information).

Concerning pore volume proportion, MBC was primarily microporous, predominantly featuring micropores smaller than 2 nm. The average micropore volume ratio (V_{micro}/V_{total}) exceeded 60%, with a maximum of 72% dedicated to micropores. The zenith of microporous pore volume (V_{micro}) was observed for WKM900-CO_2, reaching 0.34 cm^3/g, where the maximum internal SSA ($S_{\alpha s,inter}$) of 1172 m^2/g was also observed. Similarly, KB also falls within the domain of microporous materials; for example, KB850-CO_2 exhibited V_{micro}/V_{total}=72% with the highest V_{micro} of 0.31 cm^3/g and $S_{\alpha s,inter}$ of 848 m^2/g. It is conjectured that although both WKM and KB are categorized as algae, slight disparities in micromorphology or elemental composition would lead to nuanced distinctions in the optimal carbonization temperature for maximizing the porosity of the derived MBC.

Figs. 4 and **S2** in the Supporting Information depict the PSD curves of carbonized WKM and KB samples, respectively. The visibility of micropores and mesopores in MBC increased by post-water washing and CO_2 aeration, elucidating their development during MB carbonization. Initially, N_2 molecule access to these pores was hindered by water-soluble obstacles, which were removed through washing processes. A conspicuous peak in the range of approximately 1.1–1.4 nm, accompanied by a relatively subdued peak at 1.9–2.0 nm, signified the presence of micropores. Additionally, a well-defined peak at 3.8–3.9 nm indicates the existence of mesopores. The hierarchical porous structure of MBC positions it as a promising candidate for diverse industrial applications. Micropores offer active sites for catalysis, electrochemical storage, and other reactions, while mesopores facilitate multiphase flux transfer processes. This distinctive porosity enhances the material's utility across various industrial applications.

Derived from the comprehensive pore structure data, it is reasonable to infer that surface etching reactions conducive to pore formation took place during the carbonization of MB. The intensity of these reactions was contingent upon the carbonization temperature. Additionally, it became apparent that unidentified water-soluble substances introduced pore-blocking effects, which can be mitigated through washing methods, unveiling the inherent porous structure of MBC. Subsequent investigations were undertaken into the mechanisms governing pore formation and revelation through XRF, TGA, and SEM-EDS characterizations.

3.3 Investigating mechanisms of intrinsic pore development and unveiling in MBCs

TGA proves valuable in exploring the thermal degradation characteristics of raw materials and the pyrolysis products. Raw-WKM and Raw-KB exhibited substantial mass loss below 400 °C due to the thermal decomposition of MB tissues, including alginic acid (see **Fig. S3** in the Supporting Information). MBC did not display such mass loss. Except for WKM1000, KB950, and KB1000, however, all other samples demonstrated noticeable mass loss at higher temperatures, particularly above 800 °C. The high-temperature mass loss diminished progressively with increasing carbonization temperature, culminating in almost no mass loss for the WKM1000, KB950, and KB1000 samples. This implies that vaporizable impurities in WKM fully evaporated between 950 °C and 1000 °C, while for KB, this occurred between 900 °C and 950 °C.

For a comprehensive understanding of the impurities evaporated

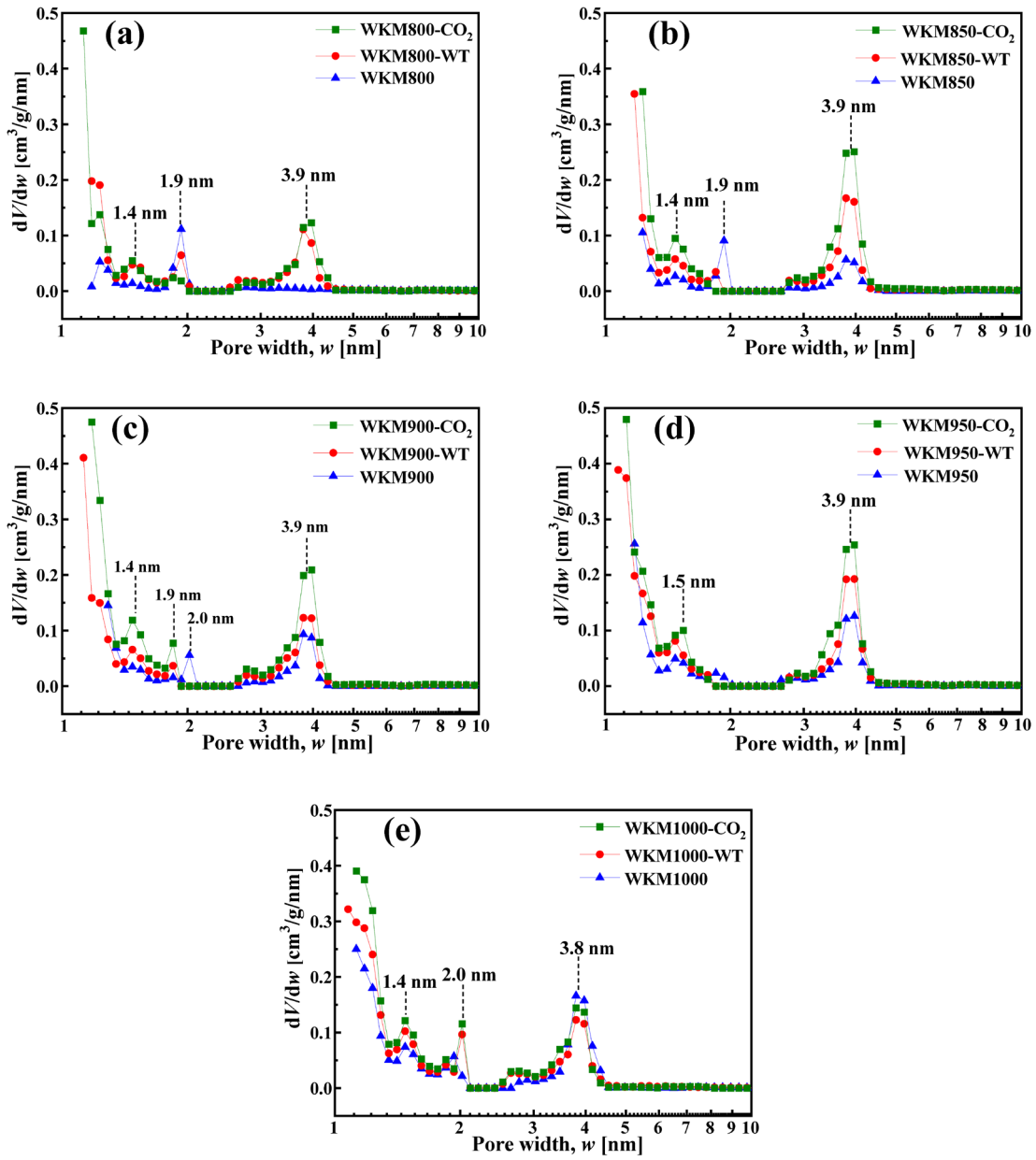

Fig. 4 PSD of WKMx, WKMx-WT, and WKM-CO_2 prepared at various carbonization temperatures: (a) 800 °C, (b) 850 °C, (c) 900 °C, (d) 950 °C, and (e) 1000 °C.

during the carbonization process, XRF elemental analysis plays a pivotal role. This analysis offers quantitative insights into material composition, elucidating elemental changes based on carbonization temperature. As outlined in **Table 2**, carbonized WKM samples displayed substantial hetero-elements, primarily comprising Na, Mg, K, Ca (alkali and alkaline earth metals (AAEMs)), and Cl. These hetero-elements are intrinsic to raw WKM (see **Table 2**). With an escalation in carbonization temperature, the Na and Cl contents of WKM-derived MBC gradually decreased, while the K content remained relatively stable up to 950 °C. At 1000 °C (WKM1000), the Na and Cl contents remarkably reduced to 0.4 mass% and 1.0 mass%, respectively, from 8.7 mass% and 6.1 mass% of WKM800. The K content also slightly decreased to 1.4 mass% from 2.0 mass% of WKM800. Unlike Na, K, and Cl, Mg and Ca exhibited an increasing trend at higher carbonization temperatures, as the elemental compositions are relative values; decreases in other elements' contents induced a noticeable rise in Mg and Ca contents. Similar patterns were observed in the KB samples, with detailed data in **Table S2** of the Supporting Information. The XRF results indicate that the observed mass loss above 800 °C in the TGA results was attributed to the gasification of Na, K, and Cl species.

The elemental changes should correspond to the development of the intrinsic porous structure of MBC. Potassium compounds are recognized as effective activation agents for carbon materials used in preparing highly microporous AC [32]. Inherent K species in MB play a crucial role in creating micropores in MBC. Conversely, substances like NaCl and $CaCl_2$ likely assist K species in mesopore formation [33, 34]. Gasification of these elements at 850–950 °C causes

Table 2 XRF elemental compositions (mass%) of raw MB, MBC, and treated MBC samples derived from WKM.

Sample	CHNO	Other elements						
		Na	Mg	K	Ca	P	S	Cl
Raw-WKM	84.5	5.4	1.2	1.3	1.5	0.2	0.7	5.0
WKM800	77.2	8.7	2.1	2.0	2.5	0.3	1.1	6.1
WKM850	76.1	8.3	2.4	2.1	2.9	0.3	1.2	6.7
WKM900	80.0	6.6	2.4	1.7	2.8	0.3	1.0	5.2
WKM950	80.2	4.6	3.3	2.0	3.9	0.5	1.5	4.0
WKM1000	87.6	0.4	3.5	1.4	4.1	0.5	1.5	1.0
WKM800-WT	90.6	—	4.1	0.1	3.1	0.6	1.3	0.2
WKM850-WT	90.5	0.1	4.0	0.1	3.7	0.5	1.0	0.1
WKM900-WT	90.3	0.1	3.9	0.1	3.3	0.6	1.3	0.1
WKM950WT	90.2	—	4.3	—	3.7	0.7	1.1	—
WKM1000-WT	91.2	—	4.1	—	3.1	0.4	1.2	—
WKM800-CO_2	94.7	—	2.0	—	1.7	0.3	1.2	—
WKM850-CO_2	95.5	—	1.0	—	1.3	0.5	1.7	—
WKM900-CO_2	94.2	—	1.5	—	1.7	0.6	2.0	—
WKM950-CO_2	95.5	—	1.1	—	1.3	0.5	1.6	—
WKM1000-CO_2	95.4	—	1.4	—	1.2	0.2	1.8	—

—: Undetected.

continuous etching reactions with the carbon surface, resulting in numerous pore structures [35–37]. These impurity species in MB serve a dual role: acting as a self-holding activation agent to introduce the intrinsic porous structure in MBC and hypothesized to induce a pore-blocking effect. Carbonization at 1000 °C is believed to cause partial evaporation of such pore-blocking species. This is evident in the decreased Na, K, and Cl contents of WKM1000 and KB1000 (**Tables 2** and **S2** in the Supporting Information). Consequently, intrinsic latent pores are partially alleviated, as seen in increased pore structural parameters (**Tables 1** and **S1** in the Supporting Information).

Post-washing treatments of MBC validated the hypothesis. A straightforward pure water-washing method was initially employed to eliminate these minerals. After water washing, the contents of Na, K, and Cl became negligible (**Table 2**), accompanied by a notable increase in porosity (**Table 1**) for all WKM samples (WKMx-WT). Similar outcomes were observed for KB-derived samples (see **Tables S1** and **S2** in the Supporting Information). Conversely, the average contents of Mg and Ca in the WKMx-WT samples remained at 4.0 mass% and 3.5 mass%, respectively, with a minimal decrease after water washing. Correspondingly, the residual contents of Mg and Ca in the KB-derived carbons post-water washing (KBx-WT) were also substantial, at 3.9 mass% for Mg and 3.1 mass% for Ca (**Table S2** in the Supporting Information). These findings indicate that Na, K, and Cl species are water-soluble and can be effectively removed by pure water washing, while Mg and Ca species cannot be eliminated through this method.

Hence, the CO_2 aeration washing method, known for its efficacy in removing Mg and Ca compounds from MBC [28], was employed as an alternative to eliminate the remaining minerals. The higher removal efficacy of Mg and Ca compounds by the CO_2 aeration washing method, compared to the pure water-washing method, can be attributed to chemical conversions from lower solubility salts (such as hydroxides and carbonates) to higher solubility hydrogen carbonates in the presence of excess dissolved CO_2 [28]. Following CO_2-aerated washing, Mg and Ca contents decreased to an average of 1.4 mass% and 1.5 mass% for carbonized WKM samples (**Table 2**, WKMx-CO_2) and 1.6 mass% and 1.4 mass% for carbonized KB samples (**Table S2** in the Supporting Information, KBx-CO_2), respectively, signifying substantial improvements. Notably, this process stands out for its simplicity, cost-effectiveness, and environmental friendliness, as it avoids additional chemical emissions. Deep cleaning with CO_2-aerated water further eliminated the pore-blocking effect, revealing more hidden intrinsic pores of MBC (**Tables 1** and **S1**). Overall, XRF analysis confirms that the water washing and CO_2 aeration washing methods effectively removed pore-blocking minerals from MBC, enhancing the quality and purity of the final MB-derived porous carbon products.

SEM-EDS analysis was conducted on MBC before and after washing treatments to further confirm the removal of pore-blocking species. **Fig. 5**(a) and (d) reveal granular substances such as crystals on the surface of MBC. Following water washing, most of these particles were eliminated, exposing the porous surface of MBC (**Fig. 5**(b) and (e)). In contrast, CO_2 aeration washing resulted in the near absence of mineral particles on the surface, revealing the three-dimensional (3D) honeycomb structure of WKM and the multilayer structure of KB clearly (**Fig. 5**(c) and (f)).

Coupled energy-dispersive X-ray spectroscopy (EDS) unveiled that the elements constituting the surface particles of unwashed MBC samples were Na, Mg, K, Ca, and Cl (**Table 3** and **Fig. S4** in the Supporting Information). Only 48.2 mass% and 51.2 mass% of carbon were detected at the surface of WKM900 and KB900, respectively. Substantial reductions in Na, K, and Cl contents at the surface were observed after water washing. More carbon elements were exposed within the EDS scanning range, reaching 90.0 mass% for WKM900-

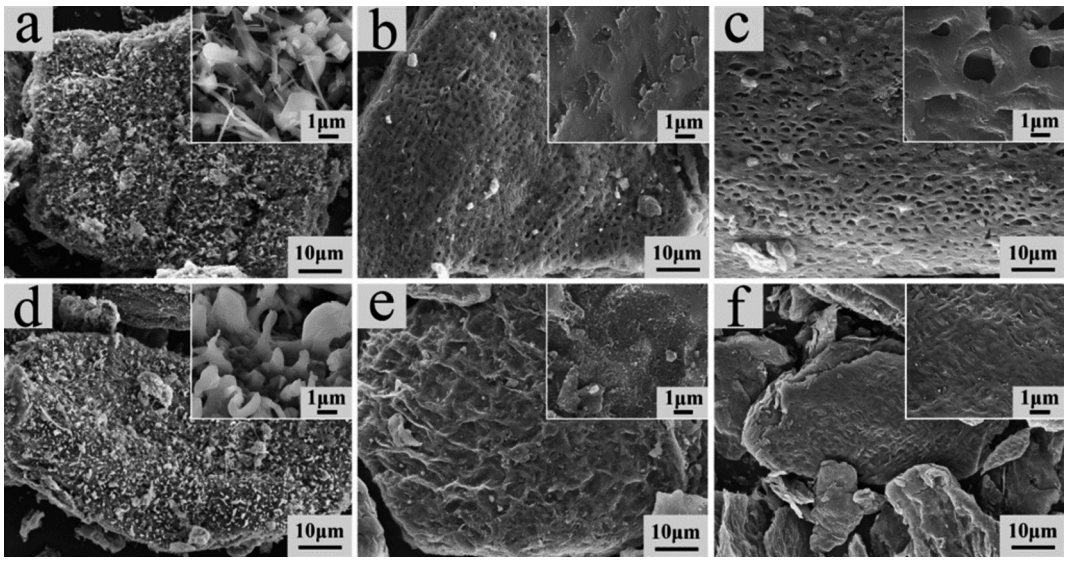

Fig. 5 SEM images of (a) WKM900, (b) WKM900-WT, (c) WKM900-CO_2, (d) KB900, (e) KB900-WT, and (f) KB900-CO_2. Insets: High-magnification images.

Table 3 EDS elemental compositions (mass%) of MBC samples before and after washing treatments.

Sample	C	Other elements				
		Na	Mg	K	Ca	Cl
WKM900	48.2	16.9	1.8	8.1	6.4	18.4
WKM900-WT	90.0	0.2	5.9	0.2	3.3	0.3
WKM900-CO_2	98.5	0.0	0.2	0.1	0.9	0.2
KB900	51.2	15.4	2.6	6.8	9.0	14.9
KB900-WT	86.7	0.2	7.7	0.3	4.9	0.2
KB900-CO_2	94.8	0.1	1.9	0.1	2.7	0.4

WT and 86.7 mass% for KB900-WT. A substantial amount of Mg and Ca remained on the surface. Utilizing the CO_2 aeration washing method eliminated most of the Mg and Ca from the surface, resulting in a high carbon content of 98.5 mass% for WKM900-CO_2 and 94.8% for KB900-CO_2. The EDS results aligned with the XRF results, signifying the effective removal of pore-blocking mineral species from the outer surface and the inner part of the MBC particles.

The internal morphology of MBC was examined *via* SEM from an interstice. WKM800-WT and KB800-WT were chosen as representative samples for SEM analysis, allowing for clear observation due to water washing. WKM800-WT exhibited an internal structure resembling a 3D honeycomb pattern (**Fig. S5**(a) in the Supporting Information). Upon closer examination of the high-magnification diagram, the wall thickness of the honeycomb structure was approximately 10–50 nm (**Fig. S5**(a') in the Supporting Information). The 3D honeycomb structure could offer ample spatial support for the pores on the carbon surface, enhancing its adsorption capacity [38, 39]. The honeycomb configuration is also expected to confer high compressive strength to the carbon block, ensuring stability in applications such as adsorbents [40] and electrode materials [41].

Fig. S5(b) and (b') in the Supporting Information depict SEM images of the inner part of KB800-WT, revealing its composition of multiple layers of carbon sheets, each with a thickness of approximately 5–20 nm. This multilayer structure also provides valuable spatial support for the pores on the carbon surface. Additionally, channels between the layers facilitate high-speed flux, suggesting the potential of KB-derived porous carbons for applications in heterogeneous catalysis or ion adsorption [42]. These distinctive morphological characteristics broaden the scope of potential applications for porous MBCs. However, it is essential to note that these unique characteristics may serve as prerequisites for endowing MBCs with abundant pore structures.

Combining results from various analytical techniques, **Fig. 6** depicts a possible mechanism illustrating the porosity changes in MBC through mineral removal. SEM and EDS analyses exposed mineral crystals covering the surface of carbonized WKM and KB samples, resulting in relatively low porosity. Water washing substantially removed minerals from outer and inner surfaces, corroborated by XRF, SEM, and EDS findings. This removal unveils a portion of the hidden intrinsic pore structure, leading to substantial increases in SSA and pore volume. The CO_2 aeration washing method further removed surface minerals, achieving an SSA higher than 1000 m^2/g without the usage of extraneous activating agents. These observations establish a direct correlation between elemental composition and pore structure.

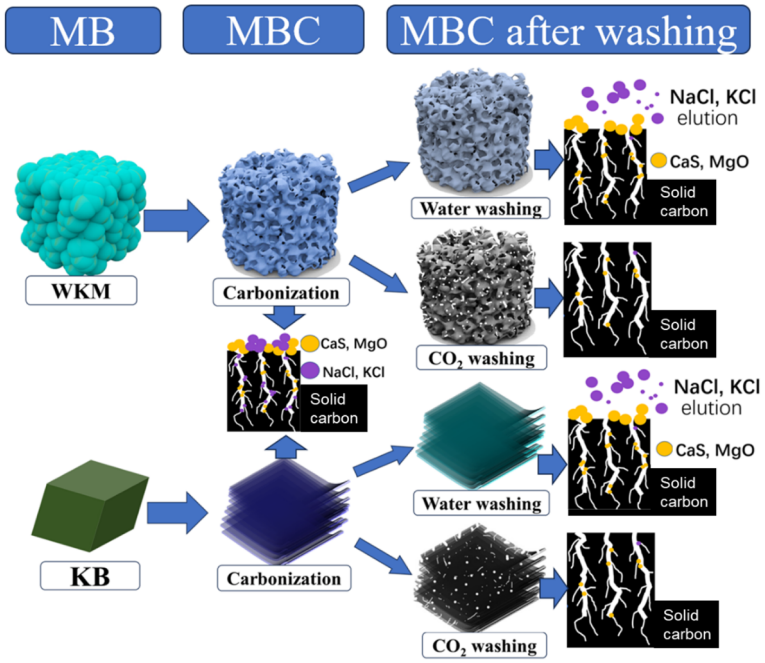

Fig. 6 Mechanism of hierarchical pore release in MBC.

Pore structure formation is attributed to catalytic activation reactions during pyrolysis by minerals containing AAEMs and Cl naturally present in MB. However, these mineral crystals cover the surface and obstruct the pores of carbonized MB samples, impeding the release of pore structures and resulting in lower porosity. The washing techniques in this study effectively released a substantial number of minerals, unveiling the underlying pore structure. While these mineral elements contributed to the pore-blocking effect, their catalytic role during pyrolysis was also pivotal for pore structure formation in MBC. This dual role contributed to positive outcomes in terms of MBC porosity. Ultimately, this study establishes an environmentally benign production process for porous carbon materials.

4. Conclusion

MB possesses a unique and highly efficient natural photosynthetic CO_2 fixation capability, surpassing other biomasses. MB-derived carbon (MBC) initially appears nonporous post-carbonization, but water washing unveils a concealed microporous and mesoporous structure. XRF, SEM, and EDS analyses validate that water washing nearly eliminates Na, K, and Cl elements. CO_2 aeration washing further aids in removing Mg and Ca, resulting in a substantial increase in C element content to 95%, thereby elevating the quality and purity of the final MBC product. The removal of these species induces a notable increase in SSA and pore volume, signifying the pore-blocking effect of these species. Simultaneously, these species contribute to the development of intrinsic pores in MBCs without the addition of extraneous activation agents. Maximizing the dual role of innate species in MB allows for the production of porous MBC. Furthermore, the CO_2 aeration washing method, emitting zero chemical pollutants, can utilize CO_2 emitted from industries, thereby promoting the development of the carbon capture industry. Coupled with MB's CO_2 fixation characteristic during its growing period, this proposed strategy highlights the potential of MBC in the environmentally friendly porous carbon industry. Optimization of carbonization and elements removal processes is challenges for the future to produce higly porous MBC with distinctive pore structure from MB species with diverse characteristics of elemental composition and micromorphology.

Supporting Information Available

Fig. S1. N_2 adsorption and desorption isotherms at 77 K for KBx, KBx-WT and KB-CO_2 at varied carbonization temperatures and comparative analysis of internal SSA using the α_S-plot method for all KB-derived samples.

Fig. S2. PSD of KBx, KBx-WT and KB-CO_2 prepared at various carbonization temperatures.

Fig. S3. TGA curves in N_2 of Raw-WKM, WKMx, Raw-KB, and KBx samples.

Fig. S4. SEM images in EDS scanning range and EDS spectra of WKM900, WKM900-WT, WKM900-CO_2, KB900, KB900-WT, and KB900-CO_2.

Fig. S5. Morphological and structural characterization of MBC: SEM images of WKM800-WT and KB800-WT at low and high magnifications.

Table S1. Pore structural parameters estimated from N_2 adsorption isotherms at 77 K of KB-derived samples.

Table S2. XRF elemental compositions (mass%) of carbonized samples of KB.

Acknowledgements

This paper presents the results obtained from Project JPNP14004, which was commissioned by the New Energy and Industrial Technology Development Organization (NEDO).

References

[1] L. Lei, L. Gu, X. Zhang, Y. Su, Catalytic oxidation of highly concentrated real industrial wastewater by integrated ozone and activated carbon, Appl. Catal. A 327 (2007) 287–294.

[2] Z. Shen, X. Xing, S. Wang, M. Lv, J. Li, T. Li, Effect of K-modified blue coke-based activated carbon on low temperature catalytic performance of supported Mn–Ce/activated carbon, ACS Omega 7 (2022) 8798–8807.

[3] S. Chen, Y. Guo, J. Zhang, Y. Guo, X. Liang, $CuFe_2O_4$/activated carbon adsorbents enhance H_2S adsorption and catalytic oxidation from humidified air at room temperature, Chem. Eng. J. 431 (2022) 134097.

[4] E.I. Ugwu, J.C. Agunwamba, A review on the applicability of activated carbon derived from plant biomass in adsorption of chromium, copper, and zinc from industrial wastewater, Environ. Monit. Assess. 192 (2020) 240.

[5] M. Gayathiri, T. Pulingam, K.T. Lee, K. Sudesh, Activated carbon from biomass waste precursors: Factors affecting production and adsorption mechanism, Chemosphere 294 (2022) 133764.

[6] G. Jaria, V. Calisto, V.I. Esteves, M. Otero, Overview of relevant economic and environmental aspects of waste-based activated carbons aimed at adsorptive water treatments, J. Clean. Prod. 344 (2022) 130984.

[7] M. Mariana, A.K. H.P.S, E.M. Mistar, E.B. Yahya, T. Alfatah, M. Danish, M. Amayreh, Recent advances in activated carbon modification techniques for enhanced heavy metal adsorption, J. Water Process Eng. 43 (2021) 102221.

[8] T.S. Saleh, A.K. Badawi, R.S. Salama, M.M.M. Mostafa, Design and development of novel composites containing nickel ferrites supported on activated carbon derived from agricultural wastes and its application in water remediation, Materials 16 (2023) 2170.

[9] A. Omri, M. Benzina, N. Ammar, Preparation, modification and industrial application of activated carbon from almond shell, J. Ind. Eng. Chem. 19 (2013) 2092–2099.

[10] D. He, Z.-H. Huang, M.-X. Wang, Porous nitrogen and oxygen co-doped carbon microtubes derived from plane tree fruit fluff for high-performance supercapacitors, J. Mater. Sci. Mater. Electron. 30 (2019) 1468–1479.

[11] Y. Li, C. Li, H. Qi, K. Yu, C. Liang, Mesoporous activated carbon from corn stalk core for lithium ion batteries, Chem. Phys. 506 (2018) 10–16.

[12] L. Ren, S. Zhou, T. Peng, X. Ou, A review of CO_2 emissions reduction technologies and low-carbon development in the iron and steel industry focusing on China, Renew. Sustain. Energy Rev. 143 (2021) 110846.

[13] H. Yi, K. Nakabayashi, S.-H. Yoon, J. Miyawaki, Pressurized physical activation: A simple production method for activated carbon with a highly developed pore structure, Carbon 183 (2021) 735–742.

[14] H. Yi, K. Nakabayashi, S.-H. Yoon, J. Miyawaki, Study on the applicability of pressurized physically activated carbon as n adsorbent in adsorption heat pumps, RSC Adv. 12 (2022) 2558–2563.

[15] X. Dong, X. Liu, H. Chen, X. Xu, H. Jiang, C. Gu, Q. Li, S. Qiao, X. Zhang, Y. Hu, Hard template-assisted N, P-doped multifunctional mesoporous carbon for supercapacitors and hydrogen evolution reaction, J. Mater. Sci. 56 (2021) 2385–2398.

[16] V. Duraisamy, S. Venkateshwaran, R. Thangamuthu, S.M. Senthil Kumar, Hard template derived N, S dual heteroatom doped ordered mesoporous carbon as an efficient electrocatalyst for oxygen reduction reaction, Int. J. Hydrog. Energy 47 (2022) 40327–40339.

[17] B. Sun, G. Li, X. Wang, Facile synthesis of microporous carbon through a soft-template pathway and its performance in desulfurization and denitrogenation, J. Nat. Gas Chem. 19 (2010) 471–476.

[18] Z. Liang, H. Xia, H. Liu, L. Zhang, J. Zhou, H. Li, W. Xie, Enhanced capacitance characteristic of microporous carbon spheres through surface modification by oxygen-containing groups, Results Phys. 15 (2019) 102586.

[19] Z. Liang, H. Liu, J. Zeng, J. Zhou, H. Li, H. Xia, Facile synthesis of nitrogen-doped microporous carbon spheres for high performance symmetric supercapacitors, Nanoscale Res. Lett. 13 (2018) 314.

[20] W. Fu, A. Chaiboonchoe, B. Khraiwesh, M. Sultana, A. Jaiswal, K. Jijakli, D.R. Nelson, A. Al-Hrout, B. Baig, A. Amin, K. Salehi-Ashtiani, Intracellular spectral recompositioning of light enhances algal photosynthetic efficiency, Sci. Adv. 3 (2017) e1603096.

[21] A.J. Simkin, L. Kapoor, C.G.P. Doss, T.A. Hofmann, T. Lawson, S. Ramamoorthy, The role of photosynthesis related pigments in light harvesting, photoprotection and enhancement of photosynthetic yield in planta, Photosynth. Res. 152 (2022) 23–42.

[22] Z. Liu, Y.G. Adewuyi, S. Shi, H. Chen, Y. Li, D. Liu, Y. Liu, Removal of gaseous Hg^0 using novel seaweed biomass-based activated carbon, Chem. Eng. J. 366 (2019) 41–49.

[23] J. Li, Y. Qiao, X. Chen, P. Zong, S. Qin, Y. Wu, S. Wang, H. Zhang, Y. Tian, Steam gasification of land, coastal zone and marine biomass by thermal gravimetric analyzer and a free-fall tubular gasifier: Biochars reactivity and hydrogen-rich syngas production, Bioresour. Technol. 289 (2019) 121495.

[24] S. Boubakri, M.A. Djebbi, Z. Bouaziz, P. Namour, A. Ben Haj Amara, I. Ghorbel-Abid, R. Kalfat, Nanoscale zero-valent iron functionalized Posidonia *oceanica* marine biomass for heavy metal removal from water, Environ. Sci. Pollut. Res. Int. 24 (2017) 27879–27896.

[25] S.E.M. Pourhosseini, O. Norouzi, H.R. Naderi, Study of micro/macro ordered porous carbon with olive-shaped structure derived from *Cladophora glomerata* macroalgae as efficient working electrodes of supercapacitors, Biomass Bioenerg. 107 (2017) 287–298.

[26] Y. Gao, R. Sun, A. Li, G. Ji, *In-situ* self-activation strategy toward highly porous biochar for supercapacitors: Direct carbonization of marine algae, J. Electroanal. Chem. 882 (2021) 114986.

[27] Y. Li, X. Liu, J. Wang, Yang, Chen, Wang, Zhang, Marine algae-derived porous carbons as robust electrocatalysts for ORR, Catalysts 9 (2019) 730.

[28] D. He, R. Sakai, K. Saito, T. Kato, C. Kosugi, H. Yi, T. Shimohara, K. Nakabayashi, S.-H. Yoon, J. Miyawaki, Facile elimination of alkali and alkaline earth metals from marine biomass-derived carbon for comparative analysis of chemical composition with standard coal and coke, Carbon 216 (2024) 118570.

[29] N. Setoyama, T. Suzuki, K. Kaneko, Simulation study on the relationship between a high resolution alpha(s)-plot and the pore size distribution for activated carbon, Carbon 36 (1998) 1459–1467.

[30] M. Thommes, K. Kaneko, A.V. Neimark, J.P. Olivier, F. Rodriguez-Reinoso, J. Rouquerol, K.S.W. Sing, Physisorption of gases, with special reference to the evaluation of surface area and pore size distribution (IUPAC Technical Report), Pure Appl. Chem. 87 (2015) 1051–1069.

[31] Pore size distribution and porosity of solid materials by mercury porosimetry and gas adsorption, Part 2: Analysis of nanopores by gas adsorption, ISO 15901-2:2022, 2022.

[32] T. Otowa, R. Tanibata, M. Itoh, Production and adsorption characteristics of MAXSORB: High-surface-area active carbon, Gas Sep. Purif. 7

(1993) 241–245.
[33] Y. Liu, W. Kang, G. Huang, Y. Liu, Z. Liu, Y. Yao, J. Jia, B. Xing, Q. Liu, C. Zhang, NaCl-assisted synthesis of porous carbons with ultra-high electrical conductivity for high-performance supercapacitors, J. Power Sources 553 (2023) 232301.
[34] G. Zhong, S. Hu, M. Xu, Z. Meng, J. Wu, X. Xu, S. Xu, X. Fu, W. Liao, S. Zheng, Y. Xu, Wheat-flour-derived magnetic porous carbons by Ca-Cl_2-activation and their application in Cr (VI) removal, ChemistrySelect 6 (2021) 13215–13223.
[35] F.-C. Wu, R.-L. Tseng, Preparation of highly porous carbon from fir wood by KOH etching and CO_2 gasification for adsorption of dyes and phenols from water, J. Colloid Interf. Sci. 294 (2006) 21–30.
[36] Y. Yang, R. Yang, C. Fan, Y. Huang, Y. Yan, Y. Zou, Y. Xu, Eucommia leaf residue-derived hierarchical porous carbon by KCl and $CaCl_2$ co-auxiliary activation for lithium sulfur batteries, Mater. Charact. 195 (2023) 112522.
[37] K. Huang, Z. Xing, L. Wang, X. Wu, W. Zhao, X. Qi, H. Wang, Z. Ju, Direct synthesis of 3D hierarchically porous carbon/Sn composites via in situ generated NaCl crystals as templates for potassium-ion batteries anode, J. Mater. Chem. A 6 (2018) 434–442.
[38] D. Zhao, S. Ge-Zhang, Z. Zhang, H. Tang, Y. Xu, F. Gao, X. Xu, S. Liu, J. Zhou, Z. Wang, Y. Wu, X. Liu, Y. Zhang, Three-dimensional honeycomb-like carbon as sulfur host for sodium–sulfur batteries without the shuttle effect, ACS Appl. Mater. Interfaces 14 (2022) 54662–54669.
[39] D. Shan, J. Yang, W. Liu, J. Yan, Z. Fan, Biomass-derived three-dimensional honeycomb-like hierarchical structured carbon for ultrahigh energy density asymmetric supercapacitors, J. Mater. Chem. A 4 (2016) 13589–13602.
[40] L. Ma, M. He, P. Fu, X. Jiang, W. Lv, Y. Huang, Y. Liu, H. Wang, Adsorption of volatile organic compounds on modified spherical activated carbon in a new cyclonic fluidized bed, Separ. Purif. Tech. 235 (2020) 116146.
[41] L.L. Xing, X. Wu, K.J. Huang, High-performance supercapacitor based on three-dimensional flower-shaped $Li_4Ti_5O_{12}$-graphene hybrid and pine needles derived honeycomb carbon, J. Colloid Interf. Sci. 529 (2018) 171–179.
[42] J. Bartelmess, S. Giordani, Carbon nano-onions (multi-layer fullerenes): chemistry and applications, Beilstein J. Nanotechnol. 5 (2014) 1980–1998.